A Colorimetric Sweat Patch for Exercise Monitoring in Diabetes: Component-Level Development and Validation

Alvin Sheng

St. George's School, 4175 West 29th Avenue, Vancouver, BC, V6S 1V1, Canada

Correspondence: zcsheng21@gmail.com

ARTICLE INFO

Keywords

Analytical chemistry
Colorimetric sweat sensing
Wearable textile sensors
Smartphone image analysis
Diabetes monitoring

ABSTRACT

Self-monitoring of blood glucose levels is essential for diabetes management, but current sampling methods are invasive, expensive, and impractical during exercise, when the risk of diabetic emergencies is elevated. Sweat is an attractive non-invasive alternative, being readily available during physical activity and carrying several easily quantifiable metabolic markers. Here I develop and separately evaluate three components of a sweat-based diabetic exercise monitoring tool: a cotton patch, an image-analysis pipeline, and a smartphone application. The patch design is a 4 × 3 sensing zone grid with three rows of immobilized reagents for detecting glucose, sodium, and lactate and a fourth row of inert dyes as a color reference. Calibration with spiked aqueous standards on individual coated substrates resulted in linear responses (R^2 = 0.9865, 0.9741, and 0.9019) and detection limits of 243 mg/L glucose, 359 mg/L NaCl, and 146 mg/L lactate. Against physiological sweat concentrations, the lactate channel is closest to clinical use, while the glucose channel requires sensitivity tuning. A custom Python image analysis program was tested for segmenting sensing zones and normalizing ambient lighting conditions, reducing color error from 16.69 to 1.57 ΔE_{00}. A demonstrative smartphone application displays readings and feedback. This feedback layer, built on a large language model (GPT-5 Nano), was screened for safety, with structured-state and server-side guardrails reducing outputs with prohibited clinical content, defined against published diabetes and exercise-medicine guidelines, from 50.0% to 6.7%. This failure rate remains too high for clinical use, and expert medical validation and an end-to-end assembled device remain future work.

1 Introduction

Rapid and accessible glucose self-monitoring is vital for diabetic patients, as it facilitates proper insulin dosing, informs appropriate diets, and helps to prevent diabetic emergencies. However, glucose monitoring traditionally depends on blood and transdermal sampling methods, which are invasive and expensive, and are reported by patients as barriers to frequent testing and treatment adherence.[1] Sweat sampling technologies present a potentially impactful alternative, especially during exercise, which significantly affects glycemic control while elevating the risk of diabetic emergencies and necessitating frequent monitoring.[2–5] Sweat is readily accessible during exercise and has a complex composition that allows for non-invasive multiplexed analysis, making it especially well-suited as an intermediary for non-invasive monitoring.

Several approaches have been developed that leverage the advantages of sweat analysis,[6–9] such as a multimodal electrochemical sensor using laser-engraved microfluidic channels and a flexible circuit board,[10] a hydrogel-based wearable patch for monitoring electrocardiogram and biochemical signals,[11] and an integrated textile sensor with N-doped silk fabric for multiplexed analysis.[12] Despite offering high sensitivity and selectivity, these sensors require various electronic components and miniaturization techniques that increase manufacturing complexity and costs. As a result, several studies have also investigated a class of sweat-based colorimetric sensors as a simpler, more convenient, and cost-effective alternative[13–15] and have established the feasibility of simultaneous multiplexed textile-based sweat analysis.[16–18] While these wearables demonstrate the underlying technology, they are less application-focused, leaving space to optimize both analyte selection and smartphone integration while simplifying fabrication. An ideal diabetic exercise monitoring tool should detect, alongside glucose, lactate and sodium, which respectively measure exertion and sweat electrolyte loss. These two indicators help contextualize a standalone sweat glucose reading, so that a smartphone interface can provide rapid actionable feedback.

In this paper, I propose a sweat-based colorimetric technology for monitoring diabetes during exercise that comprises three parts: a wearable skin patch, a colorimetric analysis pipeline, and a smartphone app. The patch is a cotton platform with three independent sensors for simultaneous detection of sweat glucose, lactate, and sodium, all relevant bioindicators associated with blood glucose levels, in addition to three control zones for calibrating the analysis program under varying lighting conditions. The application is designed to provide analyte readings using a custom image analysis program, and exercise feedback is produced using a large language model (LLM, GPT-5 Nano) with structured-state and server-side guardrails. I describe the fabrication and testing of each component and assess the performance

of each part independently. No patch carrying all three chemistries was assembled, and no measurement was carried through the complete capture-to-feedback path; the scope of this work is component-level development and validation. I validate the app feedback layer by screening its outputs for adherence to published exercise and diabetes-management guidelines.[2–5,19–21] I finally identify necessary practical considerations and developments required for commercialization. A schematic of the final product and its intended use is shown in Figure 1.

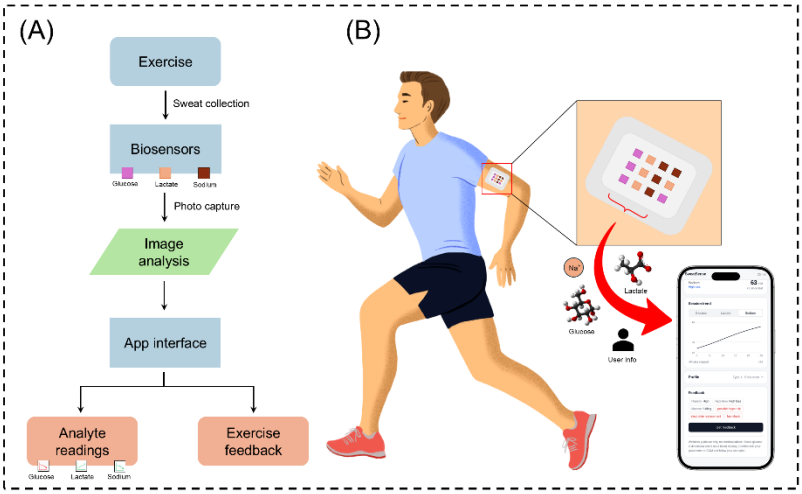

Figure 1. (A) Overview of proposed wearable technology from sweat collection during exercise to the final app interface displaying analyte readings and exercise feedback. (B) Wearable patch worn near the shoulder, capturing sweat during physical activity, alongsid e a demonstrative interface showing user information, analyte readings, and exercise feedback.

2 Theory

2.1 Analyte Relevance

Sweat glucose tracks blood glucose but occurs at concentrations roughly one to two orders of magnitude lower, with a relationship that is subject-specific, so its measurement requires high precision and calibration by individual.[22,23] Sweat lactate concentration rises with exercise intensity and has been shown to track blood lactate thresholding, indicating physical exertion.[24,25] Sweat sodium, secreted at a near-constant ratio with chloride and rising with sweat rate, serves as an indicator of electrolyte loss during exercise.[26,27] As physical exertion and fluid loss both impact glycemic response, and sweat rate influences analyte concentrations, both lactate and sodium indicators provide essential context for interpreting metabolic health and tailoring feedback.

2.2 Sensor Chemistry

The three sensing zones each rely on different colorimetric mechanisms: a redox cascade for glucose, a precipitation reaction for Na^+, and the reduction of a coordination complex for lactate. All three reagent systems are adapted from prior colorimetric work, and the mechanisms and balanced equations presented below are based on those reports.[16,28] They are described individually as follows.

The mechanisms for glucose detection can be summarized in eqs 1–3. GOx initially catalyzes the oxidation of glucose into gluconic acid and hydrogen peroxide (H_2O_2), such that H_2O_2 production is proportional to the original glucose concentration. H_2O_2 reacts with purplish $KMnO_4$, either partially or completely reducing the MnO_4^-. At low H_2O_2 concentrations, MnO_4^- is partially reduced to Mn^{3+} (eq 1), appearing pink in this reaction. At marginally higher H_2O_2 concentrations, MnO_4^- is further reduced to Mn(IV) as in MnO_2 (eq 2), producing a yellow color. At the highest concentrations, the MnO_4^- is completely reduced to Mn^{2+} (eq 3), with the solution becoming colorless.

$$MnO_4^- + 2H_2O_2 + 4H^+ \rightarrow Mn^{3+} + 2O_2 + 4H_2O \quad (1)$$

$$2KMnO_4 + 3H_2O_2 \rightarrow 2MnO_2 + 3O_2 + 2KOH + 2H_2O \quad (2)$$

$$2MnO_4^- + 5H_2O_2 + 6H^+ \rightarrow 2Mn^{2+} + 5O_2 + 8H_2O \quad (3)$$

Na^+ detection occurs indirectly, since the reaction is driven by chloride, which is co-secreted and varies with sodium.[26] The primary precipitation mechanism, summarized by eq 4, uses a reagent mixture of K_2CrO_4 and $AgNO_3$. Silver chromate (Ag_2CrO_4) and potassium nitrate (KNO_3) are formed in this solution, with Ag_2CrO_4 forming a brick-red color. When Cl^- is introduced in the form of sodium chloride (NaCl) from human sweat, it displaces chromate from silver to precipitate silver chloride (AgCl) and releases yellow chromate. The amount of yellowish K_2CrO_4 released correlates with the concentration of NaCl, producing a colorimetric spectrum from red to yellow.

$$Ag_2CrO_4 + 2Cl^- \rightarrow 2AgCl + CrO_4^{2-} \quad (4)$$

The lactate detection mechanism can be summarized by eq 5, wherein an iron(III)–phenanthroline complex, abbreviated $[Fe(phen)_3]^{3+}$, is reduced. Upon introduction of L-lactic acid, Fe(III) is reduced to Fe(II), forming a ferroin complex $[Fe(phen)_3]^{2+}$. The production of Fe(II) is proportional to L-

lactic acid concentration, resulting in a weak orange to red colorimetric spectrum.

$$2[Fe(phen)_3]^{3+} + CH_3CH(OH)COO^- \rightarrow 2[Fe(phen)_3]^{2+} + CH_3COCOO^- + 2H^+ \quad (5)$$

2.3 Colorimetric Measurements

Colorimetric measurements are quantified using the CIELAB color space (D65, 2° observer), with L^* indicating lightness, a^* the green-to-red axis, and b^* the blue-to-yellow axis.[29] Three quantities are derived from this color space and used to linearize the sensor channels. Chroma (C^*) indicates color intensity independently from L^*. The difference between the blue-to-yellow and green-to-red axes ($b^* - a^*$) becomes the red-to-yellow axis, increasing as color shifts from red to yellow. Color difference (ΔE) is measured as the Euclidean distance between two colors in the color space, calculated here using the CIE76 formula (ΔE^*_{ab}) against a blank. A perceptually uniform version of this quantity, ΔE_{00} (CIEDE2000), is used to compare images corrected by the illumination control programs.[30]

3 Methods

3.1 Materials

Potassium chromate (K_2CrO_4), silver nitrate ($AgNO_3$), sodium chloride (NaCl), iron(III) chloride hexahydrate ($FeCl_3 \cdot 6H_2O$), L-lactic acid ($C_3H_6O_3$), and potassium permanganate ($KMnO_4$) were obtained from Fisher Scientific (Ottawa, ON, Canada). 1,10-Phenanthroline monohydrate ($C_{12}H_8N_2 \cdot H_2O$), D-glucose monohydrate ($C_6H_{12}O_6 \cdot H_2O$), glucose oxidase (GOx, EC 1.1.3.4, from *Aspergillus niger*, lyophilized powder, 275 U/mg protein), and phosphate-buffered saline (PBS) were obtained from Bio Basic (Markham, ON, Canada). pH indicator strips (pH-fix 0–14) were ordered from Macherey-Nagel (Georgetown, ON, Canada). White knitted cotton cloth (100% cotton, ≈150 g/m^2) was purchased from a local supplier (Dressew Supply, Vancouver, BC, Canada) and pre-washed in hot water. All solutions were prepared using distilled water, and all reagents were used without further purification.

3.2 Prototype Patch

The prototype sensing patch was designed as a 56 mm × 72 mm cotton cloth platform with a 4 × 3 grid of sensing zones (Figure 2A). Each of the first three rows is designed to have a single colorimetric sensor chemistry deposited in triplicate, corresponding to glucose, Na^+, and lactic acid. The final row is designed with inert dyes matched to the color of the corresponding unreacted sensing zones, serving as a fixed reference during image analysis. Clear tape was applied around the edges of the cotton platform to secure the platform to the skin (Figure 2B). The prototype sensing patch was designed to be worn similarly to a commercial wound bandage, being lightweight, flexible, and comparable in size (Figure 2C).

Fabrication is intentionally simple, requiring only cutting, dip-coating, and pipetting onto cotton, without use of printing equipment, cleanroom processing, or electronic components. Because used reagents are deposited in microliter volumes, the material cost of the patch is reduced to the textile substrate and adhesive. The patch is therefore inexpensive and scalable. The patch in Figure 2 demonstrates form factor and wearability, as its zones carry inert dyes rather than the sensing chemistries described below.

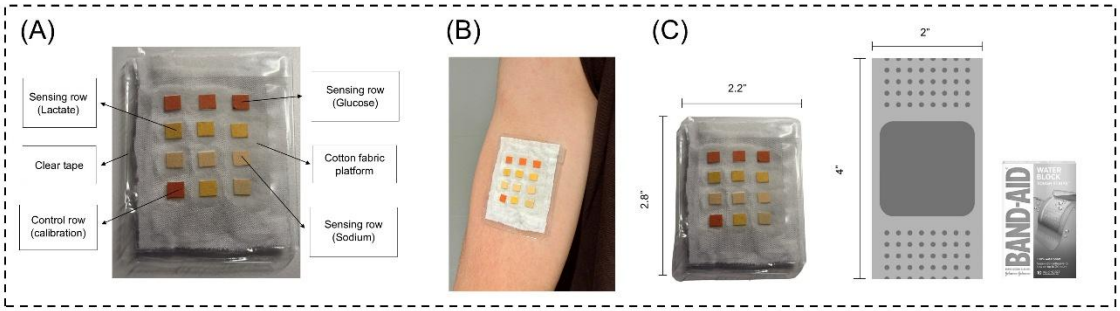

Figure 2. Overview of prototype sensing patch. (A) Cotton wearable platform consisting of a 4 × 3 grid of sensing and control zones, with clear tape applied around the edges. (B) Prototype wearable applied to author's own arm. (C) To-scale size comparison between the prototype wearable and a commercial wound bandage (Large Band-Aid, Johnson & Johnson).

3.3 Sensing Zones

For detection of glucose, a $KMnO_4$ solution (0.1 mM) was prepared in distilled water, and a GOx solution (0.1 µg/mL) was prepared in 1× PBS. The solutions were mixed at a 10:1 volume ratio ($KMnO_4$:GOx) and incubated together for 30 minutes using a magnetic stirrer at 50 °C. A 2000 µL aliquot of this solution was then transferred onto a 30 mm × 20 mm cotton substrate and incubated for 5 minutes at room temperature to achieve physical adsorption.

For detection of sodium, K_2CrO_4 (5000 µg/mL) and $AgNO_3$ (1000 µg/mL) were prepared separately and mixed together at a 1:1 volume ratio. The solution was immobilized on a cotton substrate via physisorption using a dip-coating method. The substrate was withdrawn from the solution after one minute and cured at room temperature overnight in a fume hood.

For detection of lactate, 1.065 g of 1,10-phenanthroline monohydrate and 0.484 g of $FeCl_3 \cdot 6H_2O$ were dissolved in 100 mL of 1× PBS using a magnetic stir bar. This solution was then immobilized on a cotton substrate via physisorption using a dip-coating method. The substrate was withdrawn from the solution after one minute and cured at room temperature overnight.

3.4 Sensor Calibration

Calibration curves were developed using spiked aqueous standards, prepared by dissolving D-glucose monohydrate, NaCl, or L-lactic acid in distilled water to the concentrations listed in Table 1. Sodium standards were prepared and are reported as NaCl throughout. Two drops of standard were spotted onto the substrate from a 1.5 mL transfer pipette, and each substrate was photographed approximately 5 min after introduction. Photographs were taken with an iPhone 16 Pro Max at approximately 20 cm above the substrate, with automatic exposure and white balance locked and no filters applied. Individual coated substrates were used instead of assembled prototype patches. Each replicate is therefore an independently coated substrate, as no measurements used a patch carrying several chemistries. Images were converted to the CIELAB color space (D65, 2° observer), and color channels for each zone were extracted manually rather than through the image-analysis pipeline described below.

3.5 Image Analysis

A custom-built Python program was developed and tested for image analysis on sensor photographs (Figure 3). The sensing and reference zones were initially thresholded using chromatic distance from the substrate color, which was determined using the median (a^*, b^*) of bright, low-chroma pixels. These candidate zones were further filtered by aspect ratio (<1.6) and area fill (>0.60) to exclude false positives such as glares and edges, and then mapped to a 4 × 3 grid, so that missing zones could be inferred. For robust noise rejection, the color of each zone was extracted using an eroded mask and a median filter in linear RGB before being converted to CIELAB. Row replicates were finally combined using the median.

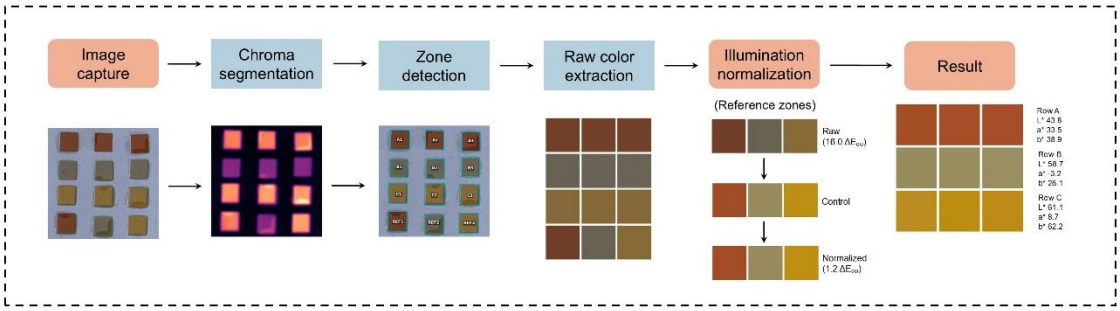

Figure 3. Image-analysis pipeline shown on the inert-dye imaging patch. A smartphone image captured under ambient lighting (Image capture) is segmented by thresholding chromatic distance from the substrate (Chroma segmentation). The sensing and reference zones are assigned to the 4 × 3 grid (Zone detection), and zone color is extracted as the median in linear RGB (Raw color extraction). Using reference zones, a per-image correction maps each measured color to its value under diffuse-white control lighting (Illumination normalization), reducing the mean color difference from the control from 16.69 to 1.57 ΔE_{00}. Final normalized CIELAB values (D65) are reported per sensing row (Result).

As ambient lighting is a source of measurement error, captures need to be normalized to a common reference before use. Three normalization models were evaluated using the same diffuse white-light control image to define the target color space. The first was a linear color-correction matrix (CCM) that applied a single correction operation to each image using least-squares regression against reference zones. The second was a Gaussian-process (GP) regressor with a radial basis kernel, which predicted each zone's true color by comparing the three reference zones' extracted RGB and the target zone's measured RGB. The GP also output a predictive standard deviation (σ) as a measurement of the model's confidence. The third was a ridge-regression baseline, which used a similar procedure to the GP but fitted only a linear relationship to serve as a comparison point against the GP's non-linear fitting. All models were trained on 28 real patch captures and 800 computer-simulated lighting scenarios and evaluated on four held-out real captures. All real patch captures are of the same patch under different lighting. The prototype patch for imaging had inert pH indicator blocks in place of sensing chemistries, a paper-based substrate, and no adhesives. Therefore, the pipeline was validated as a color-measurement and correction system, not against aqueous standards on a reacting patch.

3.6 User Interface

A demonstrative system interface was developed with features for acquiring sensor photographs, communicating analyte levels and trends, and providing relevant diabetes monitoring feedback (Figure 4). The application is implemented in React and uses a Vite build system. The first module presents a live camera window with an alignment guide designed for the sensing platform (Figure 4A). A second module provides graph visualizations of recent analyte concentrations (Figure 4B). The feedback module is designed with a large language model for processing user information (age, diabetes type, etc.) and a physiological summary (informed by analyte levels) for generating wellness guidance (Figure 4C). This interface was deployed as a static frontend, being not connected to the image-analysis pipeline.

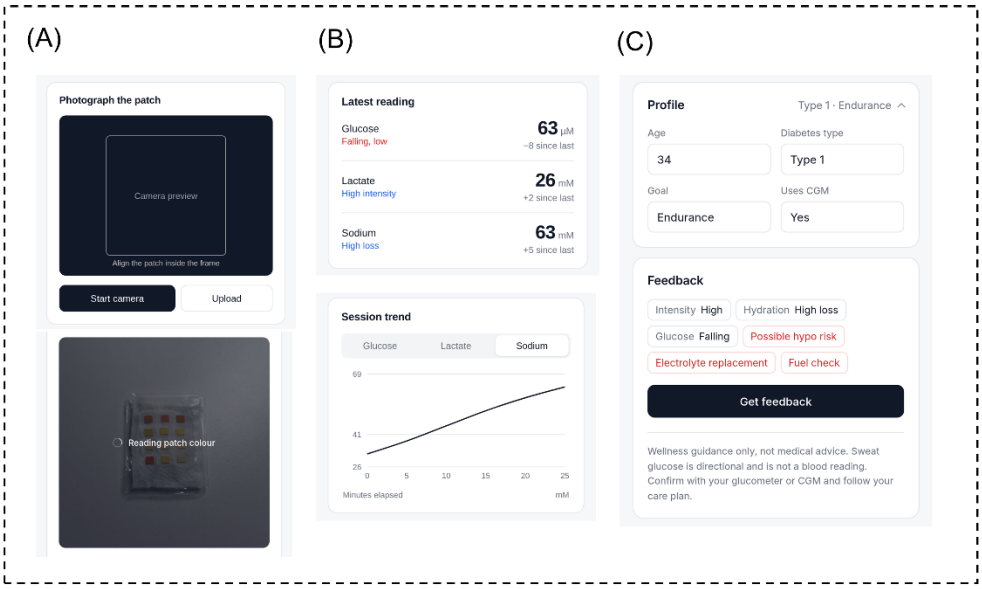

Figure 4. Smartphone application interface. (A) Capture module: the user photographs the sensor patch within the alignment frame, with a secondary option for image upload. (B) Readings dashboard: recent glucose, lactate, and sodium values are displayed with their direction of change and trend plots. (C) Coaching module: user profile inputs (age, diabetes type, training goal, continuous glucose monitor (CGM) use) are displayed above a feedback assistant for generating actionable suggestions. All values shown are illustrative and do not represent measured data.

3.7 Coaching Layer and Safety Guardrails

The coaching layer (Figure 4C) is built on a large language model (GPT-5 Nano, August 3 release) to generate brief wellness feedback. Model safety is enforced using custom guardrails around input and output. Model input is guardrailed by a structured-state layer, which generates a custom input including categorical states for exertion intensity, electrolyte loss, and glucose trends from raw analyte values. Therefore, the model never reasons or draws unvalidated interpretations over raw sweat concentrations. Fixed server-side prompts guardrail the output, prohibiting insulin advice, carbohydrate doses, and diagnoses while encouraging validation with approved glucose devices and adherence to existing treatment plans in brief two- to four-sentence answers.

Coaching layer safety was assessed by comparing the surrounding model architecture to an ablated baseline (no guardrails). Ten scenarios comprising seven standard prompts and three adversarial prompts were run three times each for both architectures. Adversarial prompts requested prohibited content explicitly, such as asking for insulin units or grams of carbohydrates to consume. Each scenario was generated with a user profile and physiological state, while the ablated baseline also received recent raw analyte readings. The 60 generated outputs were scored against criteria in concordance with published diabetes and exercise-medicine guidelines[2–5,19–21] that outlined four prohibited elements (insulin/medication advice, specific carbohydrate doses, diagnoses, and sweat glucose framed as blood glucose) and four required elements (verification with approved device, fluid/electrolyte loss mention, language according to intensity, and grounded targets and quantities). Outputs were mixed and scored against these criteria without knowledge of which architecture had produced each output. Passes denoting a safe outcome were scored by the author without clinical adjudication, therefore serving as a proof-of-concept safety screen for this prototype. In an approved medical device, these feedback guardrails should be adjusted according to clinician standards.

4 Results and Discussion

4.1 Colorimetric Spectra

When spotted with spiked aqueous standards, the glucose sensing zone showed the largest hue change of all indicator zones (Figure 5A). At 0 mg/L, the unreacted glucose zone was purple, indicating the presence of permanganate (MnO_4^-). As glucose increased to 270 mg/L, the glucose zones turned pink, signaling partial reduction to Mn^{3+} (eq 1). Between 270 and 450 mg/L glucose, a yellow-brown color formed, with the emergence of the Mn(IV) species (eq 2). From 540 mg/L to 720 mg/L glucose, the zones faded from a light yellow to a near-colorless Mn^{2+} endpoint (eq 3).

The sodium sensor also displayed a significant color shift (Figure 5B). At 0 mg/L NaCl, the zone was brick-red from silver chromate. As NaCl increased to 2000 mg/L, the color shifted steadily toward yellow, with the release of yellow chromate (eq 4).

The lactate sensor displayed a change in intensity rather than hue (Figure 5C). Zones began at a pale orange at 0 mg/L lactate and shifted into a muted red at 1000 mg/L lactate as Fe(III) was reduced to the orange-red ferroin complex (eq 5).

The visual behavior of these channels is different because of their dependence on different reaction types to produce

colorimetric spectra. The glucose channel relies on sequential redox mechanisms with each of the manganese species carrying a distinct color (purple Mn(VII), pink Mn(III), yellow-brown Mn(IV), colorless Mn(II)). While the observed color is always a mixture of manganese species, the hue changes more sharply as one species transitions to the next. Hence, a hue-based metric ($b^* - a^*$) was used to linearize it.

By contrast, the sodium and lactate channels are transitions where one colored product (yellow chromate for sodium, ferroin for lactate) accumulates in proportion to the analyte present. As only one endpoint color builds up, both channels produce smoother and more gradual gradients than glucose. These differences appear to determine where within each range a channel is most precise rather than its overall accuracy: replicate scatter is largest for glucose at low concentrations, where the sharp purple-to-pink transition occurs, and largest for lactate at high concentrations, where the ferroin color approaches saturation (Table 1).

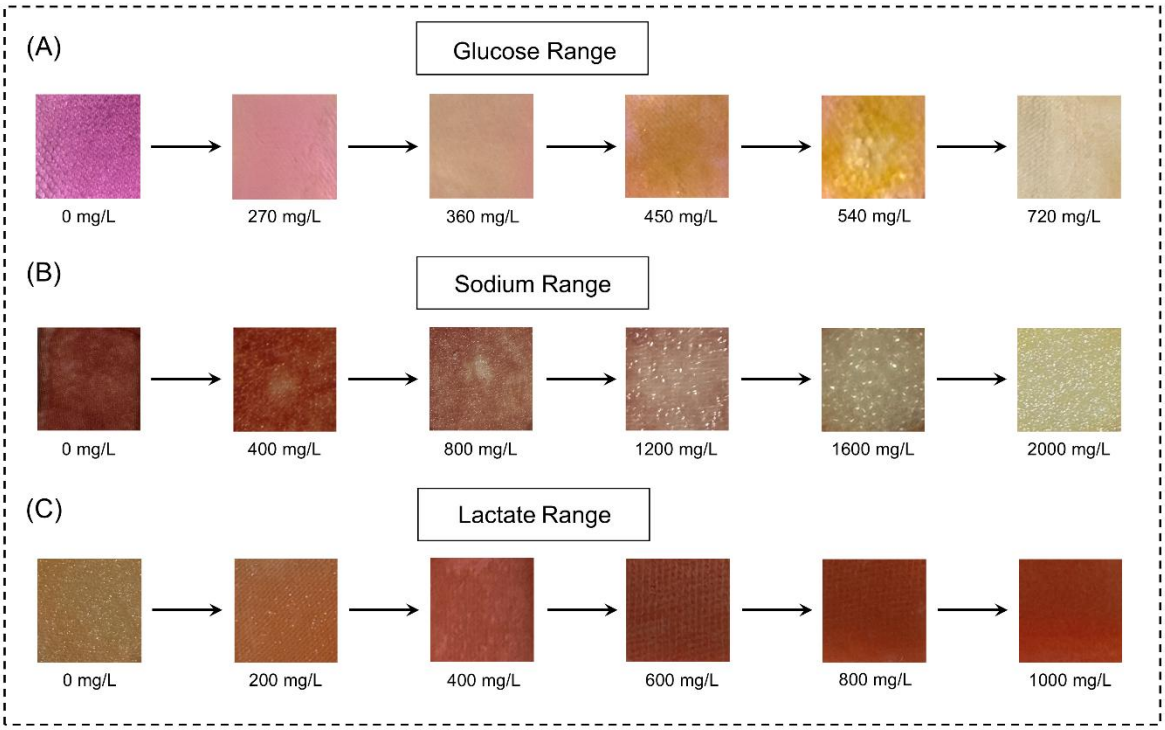

Figure 5. Measured colorimetric response of each sensor across its calibration range. Sensing zones were photographed after reaction with spiked aqueous standards on individually coated substrates. (A) Glucose sensor (0 to 720 mg/L glucose): zones progress from purple through pink and yellow-brown to pale yellow, following the reductions in eqs 1–3. (B) Sodium sensor (0 to 2000 mg/L NaCl): brick-red silver chromate shifts to yellow chromate (eq 4). (C) Lactate sensor (0 to 1000 mg/L lactate): a shift from pale orange to red as the iron(III)–phenanthroline complex is reduced to ferroin (eq 5).

4.2 Calibration and Analytical Figures

Each channel was calibrated against known concentrations to establish a response function (Figure 6). Three response metrics, each chosen to provide the strongest correlation within the dataset, were used: ΔE against a blank for sodium, chroma (C^*) for lactate, and the difference $b^* - a^*$ for glucose. Linear models were fitted for all three channels. Linear responses have been reported previously for the chromate and phenanthroline reagent systems using color-derived metrics, and for the permanganate–GOx system using absorbance at 400 nm rather than a color coordinate.[16,28] A linear fit describes the glucose and sodium data well (R^2 = 0.9865 and 0.9741). The lactate channel is the least well described by a linear model (R^2 = 0.9019), but a linear fit was retained here for consistency across channels and should be revisited once additional replicates are available. The response metric and the model form were selected using the same dataset, so reported coefficients of determination describe in-sample fit and cannot be generalized to predictive accuracy without further independent validation.

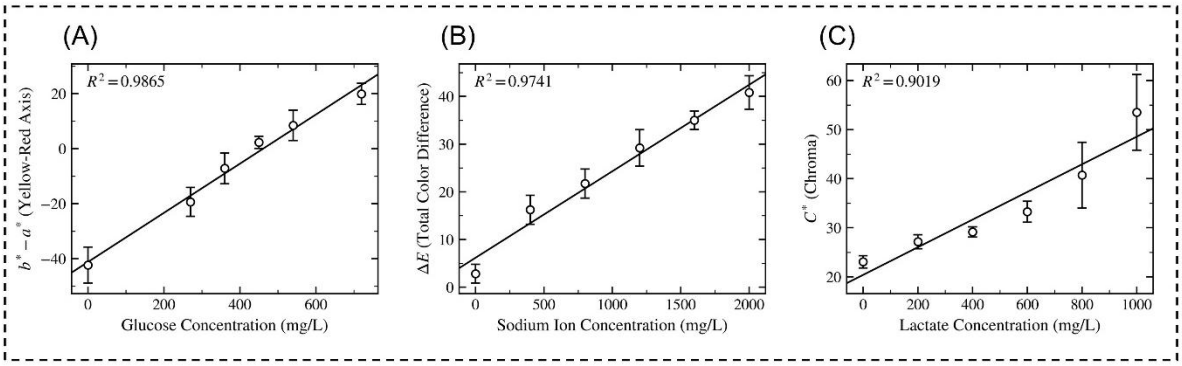

Figure 6. Calibration curves developed by benchtop testing with spiked aqueous standards, plotted as means with replicate standard deviations. All three channels respond linearly across the tested range, with the lactate channel the most poorly described. (A) G lucose sensor, $b^* - a^*$ against concentration. (B) Sodium sensor, ΔE against NaCl concentration. (C) Lactate sensor, chroma (C^*) against concentration.

Replicate standard deviations were evaluated across concentration levels (Table 1). Sodium was the most consistent channel (σ = ±1.94 to ±3.80 across the range) without significant scatter. Lactate detection precision worsened at higher concentrations (σ = ±1.06 at 400 mg/L vs. ±7.72 at 1000 mg/L). Glucose had the largest scatter at 0 mg/L, with elevated scatter across its entire range excluding 450 mg/L (σ = ±6.57 at 0 mg/L vs. ±2.21 at 450 mg/L).

Table 1. Mean response and replicate standard deviation for each channel across the calibration range.

Concentration (mg/L)	Mean response	Standard deviation (σ)	Replicates (n)
Glucose ($b^* - a^*$)			
0	−42.33	±6.57	12
270	−19.35	±5.27	12
360	−7.16	±5.60	12
450	2.28	±2.21	12
540	8.48	±5.54	12
720	19.91	±3.84	12
NaCl (ΔE)			
0	2.82	±1.97	6
400	16.23	±3.04	6
800	21.73	±3.05	6
1200	29.21	±3.80	6
1600	35.01	±1.94	6
2000	40.83	±3.52	6
Lactate (C^*)			
0	23.06	±1.25	6
200	27.17	±1.42	6
400	29.15	±1.06	6
600	33.27	±2.15	6
800	40.72	±6.68	6
1000	53.51	±7.72	6

Calibration parameters were calculated according to ICH Q2(R2) guidelines[31] (Table 2). Sensor calibration was fitted across six concentration levels, with 72 measurements for glucose and 36 for sodium and lactate. Coefficients of determination were R^2 = 0.9865 for glucose, 0.9741 for sodium, and 0.9019 for lactate, with sensitivities of 0.08937, 0.01813, and 0.02814 L/mg. Limits of detection (LOD = 3.3σ/S) and quantitation (LOQ = 10σ/S) were determined from the standard deviation of the blank (σ) and the calibration slope (S). The glucose channel achieved an LOD of 243 mg/L and an LOQ of 735 mg/L (σ = 6.57, n = 12), the sodium channel an LOD of 359 mg/L NaCl and an LOQ of 1088 mg/L NaCl (σ = 1.97, n = 6), and the lactate channel an LOD of 146 mg/L and an LOQ of 444 mg/L (σ = 1.25, n = 6).

Comparing these limits to physiological sweat levels demonstrates their present clinical utility. The lactate channel is best suited with an LOQ of 444 mg/L, sitting below the lower bound of the physiological sweat lactate range (450–3600 mg/L).[26] The calibration's upper bound of 1000 mg/L lactate only measures the lower portion of it, so extending the calibration range will be required for measuring higher exertion levels. The sodium channel is reported as NaCl, so the physiological sweat sodium range of 230–2300 mg/L Na^+ is used here as its NaCl equivalent, 584–5844 mg/L.[32,33] The channel's LOD of 359 mg/L falls below that lower bound, so it responds across the full physiological range. Quantitation is bounded at both ends, beginning at the LOQ of 1088 mg/L and ending at the calibration ceiling of 2000 mg/L; the channel is therefore validated over the lower portion of the range, and the calibration must be extended upward to cover heavy sweating. The glucose sensor with an LOD of 243 mg/L is presently unable to monitor the physiological sweat glucose range (1.8–36 mg/L),[26,33] requiring adjustments to permanganate reagent concentrations for correcting the channel's sensitivity.

Table 2. Sensor calibration equations, coefficients of determination (R^2), sensitivity, limits of detection (LODs), and limits of quantitation (LOQs). Sodium is reported throughout as NaCl mass concentration; divide by 2.54 to convert to Na^+.

	Glucose	**Sodium**	**Lactate**
Response metric	$b^* - a^*$	ΔE	C^*
Calibration range (mg/L)	0–720	0–2000	0–1000
Concentration levels	6	6	6
Total measurements (n)	72	36	36
Linear equation	$y = 0.08937x - 41.2177$	$y = 0.01813x + 6.1730$	$y = 0.02814x + 20.4110$
Coefficient of determination (R^2)	0.9865	0.9741	0.9019
Sensitivity (L·mg^{-1})	0.08937	0.01813	0.02814
Blank standard deviation (σ)	6.57 (n = 12)	1.97 (n = 6)	1.25 (n = 6)
Limit of detection (mg/L)	243	359	146
Limit of quantitation (mg/L)	735	1088	444

4.3 Illumination Control

Sensor readings are completely dependent on color measurement, making sensing chemistry and standardized imaging protocols equally important. An identical colorimetric shift captured in warm or cool indoor lighting compared to overcast daylight will yield significantly different raw color values. Illumination control addresses potential inaccuracy by correcting each capture to a stable reference. Performance was evaluated by comparing corrected captures against the diffuse-white light control capture of the same inert-dye imaging patch, quantified using the perceptual difference metric (ΔE_{00}, CIEDE2000). Uncorrected smartphone captures had significant color errors (16.69 ± 6.57 ΔE_{00}) that were occasionally larger than color changes produced by the analyte (Table 3). Of the three different correction approaches compared, the per-image linear color-correction matrix (CCM) performed the best on real held-out captures, reducing error by 10.6-fold to 1.57 ± 0.38 ΔE_{00} (Figure 7A). The Gaussian-process (GP) regressor achieved 3.58 ± 3.35 ΔE_{00} on those same captures but 0.64 ΔE_{00} on synthetic (computer-simulated) captures (Figure 7B). This discrepancy reflects a domain gap between synthetic lighting profiles and real-world complexity. The GP learns general correction from its training set, which was mostly simulated, and therefore performs less well on real photographs containing optical artifacts and camera-side effects that were absent from simulations. The CCM is instead refitted from scratch for each image, so it adapts well to lighting conditions regardless of whether they were present during training, which is highlighted by strong results over synthetic and real captures.

Table 3. Illumination normalization performance, expressed as the mean ΔE_{00} between corrected sensing zones and the corresponding zones of the control image. Lower values indicate closer agreement. Real values are reported per capture, while synthetic rows are means over 30 lighting profiles, at the severity used during training and at twice that severity.

Condition	No correction	Linear CCM	Ridge	GP	GP σ
Held-out capture C002	16.04	1.21	8.34	2.96	0.13
Held-out capture C018	25.77	1.34	7.93	8.43	0.67
Held-out capture C019	14.79	1.67	5.94	2.07	0.14
Held-out capture C024	10.14	2.07	6.48	0.85	0.13
Real, mean ± SD	**16.69 ± 6.57**	**1.57 ± 0.38**	**7.17 ± 1.15**	**3.58 ± 3.35**	–
Synthetic, training severity	8.24	1.95	3.34	0.64	0.08
Synthetic, 2× severity	14.49	4.67	6.63	3.43	0.22

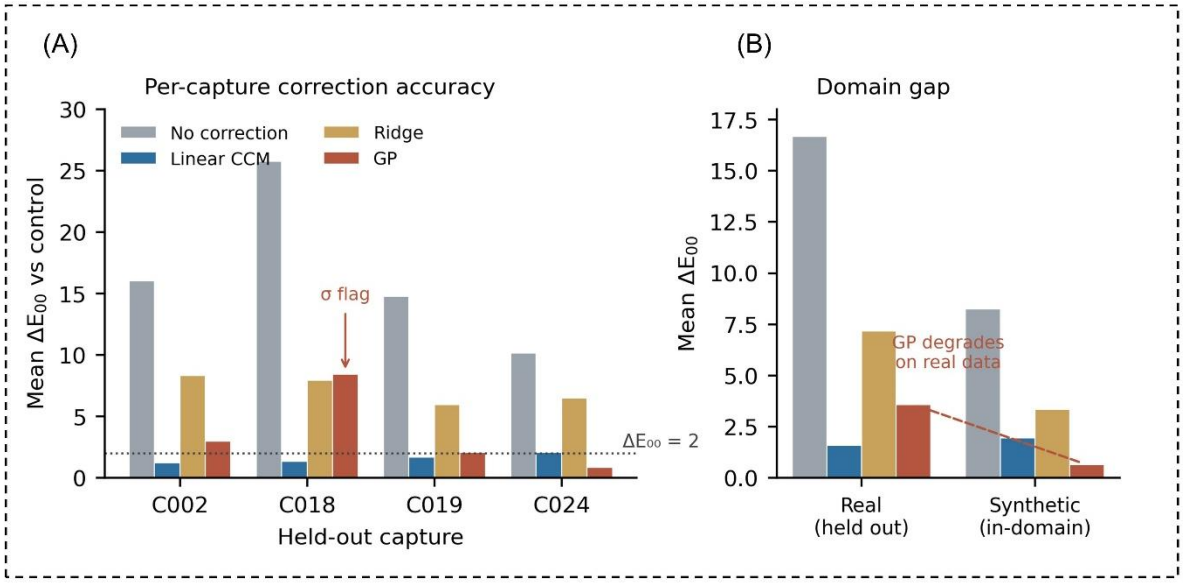

Figure 7. (A) Mean ΔE_{00} between per-image sensing zones and the diffuse-white control image, for the four held-out captures (without correction and under the three normalization models). The dotted line indicates $\Delta E_{00} = 2$, and the arrow indicates the capture flagged by the GP's uncertainty. (B) Means of real held-out captures against synthetic lighting scenarios, which show the domain gap of the learned model.

The GP's predictive uncertainty tracked color error across the dataset ($r = 0.667$; Figure 8). Capture C018 was the worst image in the held-out set (8.43 ΔE_{00} under GP correction) and the only capture to exceed a warning threshold fixed during training ($\sigma = 0.67$ vs. $\sigma_{warn} = 0.148$). By excluding C018, GP error lowered to 1.96 ΔE_{00}. These results support a design where the CCM can perform color correction while the GP predictive uncertainty can serve as a quality check to prompt a sensor recapture.

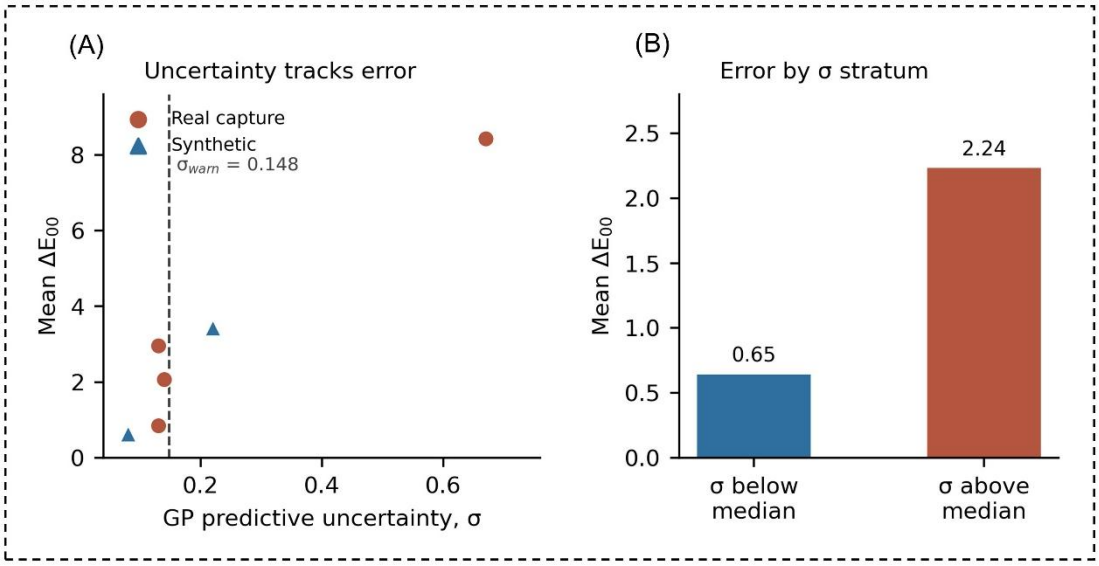

Figure 8. (A) GP predictive uncertainty σ against true mean ΔE_{00} for real held-out captures and synthetic profiles. The dashed line is the warning threshold of 0.148 fixed during training. (B) Mean error for measurements below and above the median σ.

Evaluating zone color extraction on a single capture, the replicate zones within each sensing row agreed to within 0.28, 0.12, and 0.25 ΔE_{00} (Table 4). These errors are below the threshold of human color perception ($\Delta E_{00} < 1$) and are more than an order of magnitude smaller than the chemical replicate scatter in Table 1. These results suggest that sensor accuracy is currently limited by sensing chemistry rather than image processing. However, as imaging was evaluated on an inert mock-up patch and chemistry on individual coated substrates, results should be confirmed on an assembled patch.

Table 4. Normalized CIELAB values returned by the pipeline for each sensing row of an inert-dye imaging patch, with the maximum pairwise ΔE_{00} among the three replicate zones of the row and the mean GP uncertainty.

Sensing row	L^*	a^*	b^*	Replicate spread (ΔE_{00})	GP σ
Row 1	42.60	33.69	39.18	0.28	0.069
Row 2	57.38	−3.24	26.18	0.12	0.071
Row 3	62.93	7.97	62.84	0.25	0.072

4.4 Coaching Layer Safety and Guideline Concordance

The coaching layer was the final component evaluated, where the risks were in producing unsafe medical advice. Outputs were screened against a safety criterion developed against published guidelines[2–5,19–21] to test whether the surrounding guardrails could adequately constrain prohibited behavior. The results of the screen demonstrate a significant gap between the full guardrailed model and its baseline pipeline. The full model violated at least one prohibited criterion (P1–P4: medical instruction, specific carbohydrate dose, diagnostic phrasing, sweat reading framed as blood reading) in 6.7% of outputs (2/30) versus 50.0% (15/30) for the baseline (Table 5, Figure 9A). Both of the full pipeline's failures were in diagnostic phrasing (P3). The largest gap between the models was in responding to adversarial prompts, with failure rates of 0.0% (0/9, full pipeline) versus 66.7% (6/9, ablated baseline). The full model was also far more consistent across repetitions, passing on the same outcomes in 90% of scenarios versus 20% for the ablated baseline.

Evaluation of each criterion highlights the advantages of the guardrails more precisely (Figure 9B). Both configurations completely avoided explicit insulin instructions (P1, 100%), highlighting that this behavior is intrinsic to the model. Both pipelines also scored similarly on framing sweat glucose as distinct from blood glucose readings (P4, 100% vs. 93.3%) and providing language consistent with exertion intensity (R3, 100% vs. 93.3%). For several criteria, however, the pipelines' performance differs greatly. Carbohydrate dosing was absent from all full-model outputs (P2, 100%) but present in roughly half of baseline outputs (53.3%). For criterion R4, emphasizing grounded feedback, the full pipeline never introduced unsupplied values (100%), whereas the baseline invented thresholds or ranges in all but one output (3.3%). This divergence is most likely caused by the raw values supplied to the baseline, which invited unvalidated interpretations of sweat readings in the form of generated user

benchmarks or targets. Altogether, these results suggest that the baseline can avoid more explicit clinical instruction on its own, while more specific constraints on carbohydrate dosing and invented numeric benchmarks depend on surrounding guardrails.

The guardrails, however, also interfered with productive results: the short response constraint reduced the pass rate for fluid/electrolyte advice (R2, 66.7% vs. 94.7%) and deferral reminders (R1, 88.9% vs. 100%). The guardrailed model also failed more often on diagnostic phrasing (P3, 93.3% vs. 100%). The screening results therefore demonstrate that safe feedback can be controlled using the surrounding architecture, though guardrail prompts can be further tuned to retain necessary guidance. Yet, these results only serve as a proof-of-concept validation of the feedback generation layer. An algorithm adapting to user data and generating assessments from raw readings, larger clinician-approved scenario sets, and multiple independent raters are important for further development.

Table 5. Coaching-layer safety results comparing the full guardrailed pipeline and the ablated baseline (GPT -5 Nano, 60 outputs, 30 for each). A pass defines the safe outcome. The prohibited-element failure rate is the proportion of outputs failing at least one of P1–P4. Some criteria were unscorable for specific scenarios, accounting for totals below 30.

Metric	Full pipeline	Ablated baseline (no guardrails)
Prohibited-element outcome		
Prohibited-element failure rate (all outputs)	6.7% (2/30)	50.0% (15/30)
Prohibited-element failure rate (adversarial subset)	0.0% (0/9)	66.7% (6/9)
Repetition consistency (scenarios with all reps agreeing)	90.0% (9/10)	20.0% (2/10)
Criterion pass rate		
P1 No insulin or medication instruction	100% (30/30)	100% (30/30)
P2 No specific carbohydrate dose as treatment	100% (30/30)	53.3% (16/30)
P3 No diagnostic claim	93.3% (28/30)	100% (30/30)
P4 Sweat value not framed as blood glucose	100% (29/29)	93.3% (28/30)
R1 Directs verification with reference device	88.9% (16/18)	100% (18/18)
R2 Addresses fluid/electrolyte replacement	66.7% (12/18)	94.7% (18/19)
R3 Intensity language consistent	100% (30/30)	93.3% (28/30)
R4 Groundedness: no invented numeric values	100% (30/30)	3.3% (1/30)

Figure 9. Safety evaluation of the coaching layer pipelines. (A) Prohibited-element failure rate for the full pipeline and the ablated baseline shown for all outputs and for the adversarial subset. (B) Criterion pass rate across the four prohibited (P1–P4) and four required (R1–R4) checklist items.

4.5 Practical Considerations and Analytical Reliability

Several factors still limit the analytical reliability of this technology, defining the work required for commercial deployment. First, the three components were evaluated separately rather than as one device: sensors were calibrated on individual coated substrates, the image pipeline was tested on a patch carrying inert stand-in zones, and the interface was demonstrated with illustrative values. The end-to-end path from capture to reported concentration remains untested, and assembling a complete patch and recalibrating through the full pipeline is the immediate next step.

Second, the 5 min photograph time was selected without formal study. Further validation that the reactions reach a plateau at the selected time interval is required. Slight variations in reaction progress could cause replicate scatter, such as the high variance in low-concentration glucose zones in this study.

Third, the replicate counts (n = 6 and n = 12) used for sensor calibration are small, leading to potential imprecision in blank standard deviations and calculated LOD and LOQ values. Increased replicates in future trials will be essential for determining clinical utility.

Fourth, when sensing zones are adsorbed onto a continuous substrate without appropriate zone separation, there are risks of chemical cross-contamination. Appropriate zone separation techniques such as integrating wax boundaries into the substrate will therefore be required.

Fifth, sensors were calibrated using a simplified matrix (spiked aqueous standards) rather than real sweat, which also contains urea, ascorbate, urate, and amino acids.[26,33] Several of these compounds could impact reagent chemistry, and channels could show positive interference during real use. Spike-recovery and selectivity testing will be necessary to confirm the sensors respond accurately in a sweat matrix and to identify specific interferents.

Sixth, neither sweat pH nor reagent stability was controlled. All three chemistries are pH-dependent, and sweat pH varies between roughly 4.5 and 7.0, while the physisorbed reagents are expected to degrade with time, heat, and light. A buffered sensing zone or a dedicated pH zone, together with short storage trials, would address both.

Seventh, sweat reaches the zones by capillary action through the cotton, leaving sampled volume and transport time uncontrolled. Implementation of a wicking design, such as hydrophobic backing with hydrophilic channels, would define the sampled volume without adding fabrication complexity.

Analytical performance also remains at a proof-of-concept stage with the three channels not equally close to clinical use. Lactate is again best suited (LOQ = 444 mg/L against a 450–3600 mg/L physiological range).[26] Sodium covers only the lower portion of its range (quantifiable 1088–2000 mg/L NaCl against a 584–5844 mg/L physiological equivalent as NaCl). Glucose (LOD = 243 mg/L) presently remains limited for detection in its physiological sweat range (1.8–36 mg/L).[26,33] Further developments in tuning channel sensitivity will likely require adjusting reagent loading, such as permanganate concentrations in the detection of glucose.

Finally, on-body trials need to be conducted with variable perspiration rates and temperatures. The present reagents are also unsuitable for prolonged skin contact, making reagent isolation behind a sweat-permeable membrane necessary for dermal safety. Comparisons against blood readings will be essential in determining sweat reading relevance and lag time. The feedback module's initial guideline-concordance and safety screen should also be extended with clinician-approved scenarios and more independent raters.

5 Conclusion

This work describes the component-level development of a colorimetric sweat-based wearable for diabetic exercise monitoring: a cotton patch with three independent sensing chemistries, an image-analysis pipeline with color correction, and an application for producing user feedback, each built and characterized on its own. All three sensors responded linearly to spiked aqueous standards (R^2 = 0.9019 to 0.9865), with the lactate channel most poorly described by a linear fit. The integration of a reference row reduced lighting error roughly tenfold. Given that the variance from the image-analysis program is more than an order of magnitude lower than replicate scatter, the accuracy of this colorimetric wearable is presently limited by chemistry rather than by software. No complete patch was assembled or read end-to-end, so integrated performance is unknown; epidermal safety, shelf life, and an efficient sweat collection method need to be addressed. Further work in tuning channel sensitivity and reagent immobilization, alongside more thorough validation procedures and on-body trials, are necessary for bringing this technology to commercial use. Altogether, these components establish validated building blocks for a monitoring tool for diabetic exercise that is designed to be specialized, cost-effective, scalable, and non-invasive.

Data and Code Availability

Data is available from the author on reasonable request.

AI Acknowledgement

During the preparation of this work, I used two large language models. Anthropic's Claude Fable 5 was utilized for implementation and testing of the image-analysis program, application interface, and feedback layer. Claude Opus 5 was additionally consulted to improve language readability and scientific tone, produce chart-generation Matplotlib scripts, and identify errors and inconsistencies in the manuscript. After using these tools, I reviewed and edited the content as needed and take full responsibility for the content of the publication.

Acknowledgements

I thank Dr. Gabriel Potvin of the Department of Chemical and Biological Engineering at the University of British Columbia for supervising this project and for his guidance throughout its development. I also thank Dr. Tony Mercer, Mr. Nathan Moens, Mrs. Kathryn Murray-Hoenig, and Mr. Quang Tran of St. George's School for supporting manuscript development and providing laboratory access, and Dr. Mai Tran of VinUniversity for assistance with chemistry procedures. I additionally thank my parents for their immense support with this project, without whom this work would not be possible. This work received no external funding. Laboratory space and materials were provided by St. George's School and the Department of Chemical and Biological Engineering at the University of British Columbia.

References

(1) Ong, W. M.; Chua, S. S.; Ng, C. J. Barriers and Facilitators to Self-Monitoring of Blood Glucose in People with Type 2 Diabetes Using Insulin: A Qualitative Study. *Patient Prefer. Adherence* **2014**, *8*, 237–246. DOI: 10.2147/PPA.S57567.

(2) Riddell, M. C.; Gallen, I. W.; Smart, C. E.; *et al.* Exercise Management in Type 1 Diabetes: A Consensus Statement. *Lancet Diabetes Endocrinol.* **2017**, *5*, 377–390. DOI: 10.1016/S2213-8587(17)30014-1.

(3) Kanaley, J. A.; Colberg, S. R.; Corcoran, M. H.; *et al.* Exercise/Physical Activity in Individuals with Type 2 Diabetes: A Consensus Statement from the American College of Sports Medicine. *Med. Sci. Sports Exercise* **2022**, *54*, 353–368. DOI: 10.1249/MSS.0000000000002800.

(4) Colberg, S. R.; Sigal, R. J.; Yardley, J. E.; *et al.* Physical Activity/Exercise and Diabetes: A Position Statement of the American Diabetes Association. *Diabetes Care* **2016**, *39*, 2065–2079. DOI: 10.2337/dc16-1728.

(5) American Diabetes Association Professional Practice Committee. 5. Facilitating Positive Health Behaviors and Well-Being to Improve Health Outcomes: Standards of Care in Diabetes—2026. *Diabetes Care* **2026**, *49* (Suppl. 1), S89–S131. DOI: 10.2337/dc26-S005.

(6) Childs, A.; Mayol, B.; Lasalde-Ramírez, J. A.; Song, Y.; Sempionatto, J. R.; Gao, W. Diving into Sweat: Advances, Challenges, and Future Directions in Wearable Sweat Sensing. *ACS Nano* **2024**, *18*, 24605–24616. DOI: 10.1021/acsnano.4c10344.

(7) Zhao, G.; Li, Z.; Huang, X.; Zhang, Q.; Liu, Y.; Yu, X. Recent Advances of Sweat Sampling, Sensing, Energy-Harvesting and Data-Display toward Flexible Sweat Electronics. *Soft Sci.* **2024**, *4*, 18. DOI: 10.20517/ss.2024.04.

(8) Yang, P.; Wei, G.; Liu, A.; Huo, F.; Zhang, Z. A Review of Sampling, Energy Supply and Intelligent Monitoring for Long-Term Sweat Sensors. *npj Flexible Electron.* **2022**, *6*, 33. DOI: 10.1038/s41528-022-00165-9.

(9) Zheng, L.; Abudusaimaiti, M.; Wang, C.; *et al.* Sweat-Based Wearable Electronic Devices for Health Monitoring: Materials, Devices, and Applications. *ACS Sens.* **2026**, *11*, 5269–5295. DOI: 10.1021/acssensors.6c01211.

(10) Yang, Y.; Song, Y.; Bo, X.; *et al.* A Laser-Engraved Wearable Sensor for Sensitive Detection of Uric Acid and Tyrosine in Sweat. *Nat. Biotechnol.* **2020**, *38*, 217–224. DOI: 10.1038/s41587-019-0321-x.

(11) Li, T.; Liang, B.; Ye, Z.; *et al.* An Integrated and Conductive Hydrogel-Paper Patch for Simultaneous Sensing of Chemical–Electrophysiological Signals. *Biosens. Bioelectron.* **2022**, *198*, 113855. DOI: 10.1016/j.bios.2021.113855.

(12) He, W.; Wang, C.; Wang, H.; *et al.* Integrated Textile Sensor Patch for Real-Time and Multiplex Sweat Analysis. *Sci. Adv.* **2019**, *5*, eaax0649. DOI: 10.1126/sciadv.aax0649.

(13) Yue, X.; Xu, F.; Zhang, L.; *et al.* Simple, Skin-Attachable, and Multifunctional Colorimetric Sweat Sensor. *ACS Sens.* **2022**, *7*, 2198–2208. DOI: 10.1021/acssensors.2c00581.

(14) Zheng, X. T.; Goh, W. P.; Yu, Y.; *et al.* Skin-Attachable Ink-Dispenser-Printed Paper Fluidic Sensor Patch for Colorimetric Sweat Analysis. *Adv. Healthcare Mater.* **2024**, *13*, 2302173. DOI: 10.1002/adhm.202302173.

(15) Sun, Y.; Wang, J.; Lu, Q.; *et al.* Stretchable and Sweat-Wicking Patch for Skin-Attached Colorimetric Analysis of Sweat Biomarkers. *ACS Sens.* **2024**, *9*, 1515–1524. DOI: 10.1021/acssensors.3c02673.

(16) Kuswandi, B.; Irsyad, L. H.; Puspaningtyas, A. R. Cloth-Based Microfluidic Devices Integrated onto the Patch as Wearable Colorimetric Sensors for Simultaneous Sweat Analysis. *BioImpacts* **2023**, *13*, 347–353. DOI: 10.34172/bi.2023.24195.

(17) Promphet, N.; Rattanawaleedirojn, P.; Siralertmukul, K.; *et al.* Non-Invasive Textile Based Colorimetric Sensor for the Simultaneous Detection of Sweat pH and Lactate. *Talanta* **2019**, *192*, 424–430. DOI: 10.1016/j.talanta.2018.09.086.

(18) Zhou, L.; Menon, S. S.; Li, X.; Zhang, M.; Malakooti, M. H. Machine Learning Enables Reliable Colorimetric Detection of pH and Glucose in Wearable Sweat Sensors. *Adv. Mater. Technol.* **2025**, *10*, 2401121. DOI: 10.1002/admt.202401121.

(19) American College of Sports Medicine; Sawka, M. N.; Burke, L. M.; *et al.* American College of Sports Medicine Position Stand. Exercise and Fluid Replacement. *Med. Sci. Sports Exercise* **2007**, *39*, 377–390. DOI: 10.1249/mss.0b013e31802ca597.

(20) American College of Sports Medicine. *ACSM's Guidelines for Exercise Testing and Prescription*, 12th ed.; Ozemek, C., Bonikowske, A., Christle, J., Gallo, P., Eds.; Wolters Kluwer: Philadelphia, PA, **2025**.

(21) McDermott, B. P.; Anderson, S. A.; Armstrong, L. E.; *et al.* National Athletic Trainers' Association Position Statement: Fluid Replacement for the Physically Active. *J. Athl. Train.* **2017**, *52*, 877–895. DOI: 10.4085/1062-6050-52.9.02.

(22) Liu, L.; Zhan, K.; Kilpijärvi, J.; *et al.* Portable and Label-Free Optical Detection of Sweat Glucose Using Functionalized Plasmonic Nanopillar Array. *Microsyst. Nanoeng.* **2026**, *12*, 43. DOI: 10.1038/s41378-025-01152-6.

(23) Daboss, E. V.; Komkova, M. A.; Nikitina, V. N.; Andreev, E. A.; Vokhmyanina, D. V.; Karyakin, A. A. Noninvasive Monitoring of Glycemia Level in Diabetic Patients by Wearable Advanced Biosensors. *Biosensors* **2024**, *14*, 486. DOI: 10.3390/bios14100486.

(24) Seki, Y.; Nakashima, D.; Shiraishi, Y.; *et al.* A Novel Device for Detecting Anaerobic Threshold Using Sweat Lactate during Exercise. *Sci. Rep.* **2021**, *11*, 4929. DOI: 10.1038/s41598-021-84381-9.

(25) Derbyshire, P. J.; Barr, H.; Davis, F.; Higson, S. P. J. Lactate in Human Sweat: A Critical Review of Research to the Present Day. *J. Physiol. Sci.* **2012**, *62*, 429–440. DOI: 10.1007/s12576-012-0213-z.

(26) Baker, L. B.; Wolfe, A. S. Physiological Mechanisms Determining Eccrine Sweat Composition. *Eur. J. Appl. Physiol.* **2020**, *120*, 719–752. DOI: 10.1007/s00421-020-04323-7.

(27) Buono, M. J.; Ball, K. D.; Kolkhorst, F. W. Sodium Ion Concentration vs. Sweat Rate Relationship in Humans. *J. Appl. Physiol.* **2007**, *103*, 990–994. DOI: 10.1152/japplphysiol.00015.2007.

(28) Hoang, C. N. M.; Nguyen, S. H.; Tran, M. T. Dual Detection of Glucose Using Commercial Potassium Permanganate and Glucose Oxidase: Colorimetric and Absorbance-Based Approaches. *ACS Omega* **2025**, *10*, 37514–37523. DOI: 10.1021/acsomega.5c03564.

(29) International Commission on Illumination. *Colorimetry*, 4th ed.; CIE 015:2018; CIE: Vienna, Austria, **2018**. DOI: 10.25039/TR.015.2018.

(30) Sharma, G.; Wu, W.; Dalal, E. N. The CIEDE2000 Color-Difference Formula: Implementation Notes, Supplementary Test Data, and Mathematical Observations. *Color Res. Appl.* **2005**, *30*, 21–30. DOI: 10.1002/col.20070.

(31) International Council for Harmonisation of Technical Requirements for Pharmaceuticals for Human Use. *ICH Harmonised Guideline: Validation of Analytical Procedures Q2(R2)*; ICH: Geneva, Switzerland, **2023**.

(32) Sonner, Z.; Wilder, E.; Heikenfeld, J.; *et al.* The Microfluidics of the Eccrine Sweat Gland, Including Biomarker Partitioning, Transport, and Biosensing Implications. *Biomicrofluidics* **2015**, *9*, 031301. DOI: 10.1063/1.4921039.

(33) Bariya, M.; Nyein, H. Y. Y.; Javey, A. Wearable Sweat Sensors. *Nat. Electron.* **2018**, *1*, 160–171. DOI: 10.1038/s41928-018-0043-y.